crystals

MDPI

Article

Crystallography and Surface Oxidation of Stoichiometric Arsenopyrite from Šumadija-Kopaonik Pb-Zn/Polymetallic Ore District (Serbia)

Ivana Jelić [1,*], Aleksandar Pačevski [1], Aleksandar Kremenović [1], Aleš Šoster [2,*], Andreja Šestan [3] and Janez Zavašnik [4,*]

[1] Faculty of Mining and Geology, University of Belgrade, Đušina 7, 11000 Belgrade, Serbia
[2] Department of Geology, Faculty of Natural Sciences and Engineering, University of Ljubljana, Aškerčeva Cesta 12, 1000 Ljubljana, Slovenia
[3] Centre for Electron Microscopy, Jožef Stefan Institute, Jamova Cesta 39, 1000 Ljubljana, Slovenia
[4] Gaseous Electronics Department, Jožef Stefan Institute, Jamova Cesta 39, 1000 Ljubljana, Slovenia
* Correspondence: iljubojevic@gmail.com (I.J.); ales.soster@geo.ntf.uni-lj.si (A.Š.); janez.zavasnik@ijs.si (J.Z.)

Abstract: The behaviour and stability of arsenopyrite largely depend on its crystal structure, but studies of crystallography and structural defects are scarce. For clarification, we investigated a series of natural arsenopyrite crystals from the polymetallic Pb-Zn-(±Cu,Ag,Au,Sb,Bi,W) Šumadija-Kopaonik ore district (Serbia) by powder X-ray diffraction (XRPD). Among them, samples from the Drenjak gold mineralisation showed near-stoichiometric FeAsS composition and were further investigated by conventional and high-resolution transmission electron microscopy methods. TEM revealed abundant planar crystallographic defects and epitaxial surface oxide layer formation upon air exposure. Our findings present the fundamental work on the prototype arsenopyrite structure and have further implications for studies on ion incorporation into FeAsS structure and its environmental stability and oxidation mechanisms as a source of anthropogenic As release into the environment.

Keywords: FeAsS; crystal structure; oxidation; XRPD; TEM

Citation: Jelić, I.; Pačevski, A.; Kremenović, A.; Šoster, A.; Šestan, A.; Zavašnik, J. Crystallography and Surface Oxidation of Stoichiometric Arsenopyrite from Šumadija-Kopaonik Pb-Zn/Polymetallic Ore District (Serbia). *Crystals* **2023**, *13*, 278. https://doi.org/10.3390/cryst13020278

Academic Editor: Francesco Capitelli

Received: 9 January 2023
Revised: 30 January 2023
Accepted: 1 February 2023
Published: 6 February 2023

1. Introduction

Arsenopyrite (FeAsS) is worldwide abundant natural sulphide, common in various mineral deposit types [1]. Arsenopyrite can incorporate significant amounts of metal ions, such as gold, cobalt, and nickel, either accommodated in the crystal structure in a solid solution or as micro-inclusions [2,3]. In particular, the ability of the Au incorporation renders arsenopyrite an economically relevant ore mineral and is the main reason for the extensive industry-driven research. Subjected to exploration and mining activities, arsenopyrite is also one of the main natural sources of arsenic in environmental geochemistry, presenting potential ecological concerns due to As release through sulphide weathering and oxidation.

The existing research on arsenopyrite mainly focuses on the chemistry, processing, and weathering of the Au-containing arsenic sulphide minerals [4]. The ability to incorporate Au in FeAsS structure coincides with the vast amount of (geo)chemical data published, which contrasts sharply with the available structural data [2,5–7]. The ambiguous structure of arsenopyrite has been analysed since the early days of instrumental crystallography [8] and has continued until present day [9]. Several different structural arrangements have been suggested, influenced by the method and accuracy applied in the investigation and by its similarity to marcasite (orthorhombic FeS_2, *Pnnm*) and rutile (tetragonal TiO_2, $P4_2/mnm$) prototype structures. The current consensus recognises arsenopyrite's monoclinic structure, $P2_1/c$ [9]. The published reports also highlight the possible micro-twinning and other structural defects as the main obstacle hindering the precise structure analysis, suggesting additional studies by transmission electron microscopy [10]. The basic investigations

and behaviour of arsenopyrite under TEM are rarely explored and are mostly limited to the spatial distribution of the chemical constituents, trace elements, discrete phases, and micro-inclusions [11,12].

To address these shortcomings, through X-ray powder diffraction (XRPD), we analysed a set of 14 arsenopyrite samples from polymetallic Pb-Zn-(±Cu,Ag,Au,Sb,Bi,W) mineralisations from the Šumadija-Kopaonik ore district, Serbia (Figure 1a,b), with different post-magmatic processes of deposition, mineral associations, crystallisation temperature, and chemical composition. Arsenopyrite is often present in the ores of this district and is also commonly present in the mine tailings, and all studied samples were taken from the sulphide mineralisation in which arsenopyrite represents one of the major constituents. Among investigated samples, the FeAsS samples from the Drenjak sulphide mineralisation enriched by gold [13] show only minimal variations in unit cell dimensions, d_{131} and composition, i.e., As:S ratio, with a calculated As content close to its theoretical value of 33.3 at.% [14] (Figure 1c). Arsenopyrite from other investigated localities are close to the theoretical value, but they show compositional zonation and contain considerable amounts of trace elements (e.g., Co, Ni, Sb at Sastavci, Figure 1d) or are characterised by complex mineral intergrowths and textures (Rudnik). Due to their almost ideal stoichiometry, arsenopyrite samples from Drenjak were further analysed by transmission electron microscopy, which allows atomic-scale imaging and electron diffraction obtained from the same location within the sample. Using TEM, we explored the arsenopyrite local crystal structure and symmetry, the presence of structural defects and their type, and the structure and crystallinity of the natural oxide layer formed upon exposure to air.

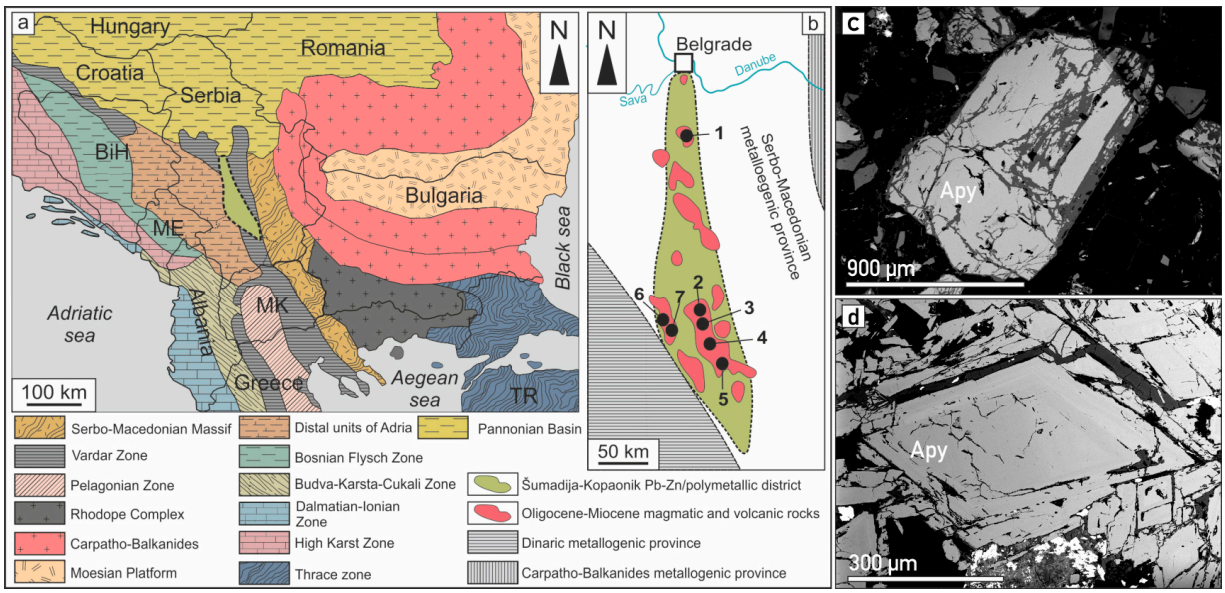

Figure 1. (**a**) Geologic structure map of Balkan Peninsula; detailed descriptions can be found in [15], regional geologic map after [16]. (**b**) Simplified schematic map of the Šumadija-Kopaonik Pb-Zn/polymetallic ore district with sampling locations: 1—Rudnik (Pb-Zn-Cu-(Ag) mine), 2—Rujak (Apy-Py veins), 3—Drenjak (Au mineralisation in Apy vein), 4—Sastavci (Pb-Zn mine), 5—Trepča (Pb-Zn mine), 6—Golijska reka (W-Mo-Bi mineralisation), 7—Jurija (W mineralisation). (**c**,**d**) SEM-BSE micrographs of characteristic arsenopyrite samples from (**c**) Drenjak and (**d**) Sastavci locations, the latter showing visible zoning due to non-homogenous chemical composition.

2. Materials and Methods

The mineralised samples and ores from the Šumadija-Kopaonik ore district were sampled in the last twenty years during several field excursions. From this sample collection curated at the Faculty of Mining and Geology in Belgrade, for the purposes of this study,

14 samples from 7 localities of different types of mineralisation (Figure 1a,b) were selected, in which arsenopyrite is one of the most abundant sulphide phases.

2.1. Scanning Electron Microscopy and Energy Dispersive X-ray Spectroscopy (SEM-EDS)

The arsenopyrite samples from the polymetallic Šumadija-Kopaonik ore district were first analysed by scanning electron microscope (SEM, JSM–6610LV, JEOL Inc., Tokyo, Japan) operating at 20 kV to determine their homogeneity and mineral association; their composition was analysed by energy-dispersive X-ray spectrometry (EDS, X-Max, Oxford Instruments PLC, Abingdon, UK), using internal standards with detection limit ~0.1 wt.%. Simultaneously, the homogeneity and possible zoning were analysed by backscattered electron (BSE) micrographs (Figure 1c,d).

2.2. X-ray Powder Diffraction (XRPD)

For X-ray Powder Diffraction (XRPD) analysis, the representative sections of the bulk samples containing FeAsS were powdered in an agate mortar. Measurements were conducted on Smartlab X-ray Diffractometer (Rigaku Co., Tokyo, Japan) in θ–θ geometry (the sample in horizontal position) in parafocusing Bragg-Brentano geometry using a D/teX Ultra 250 strip detector in 1D standard mode with Cu$K\alpha_{1,2}$ radiation source (U = 40 kV and I = 30 mA). The XRPD patterns were collected in the 5–75 °2θ range, with a step of 0.01° and a data collection speed of 2°/min. The single-crystal low-background Si sample holder was used to minimise the background signal. The unit cell parameters and d_{131} values were calculated by PDXL2-integrated X-ray powder diffraction software (Version 2.8.30; Rigaku Corporation). The characteristic arsenopyrite PXRD pattern from Drenjak, compared with the theoretical XRPD pattern from [9], is presented in Figure 2.

Table 1. X-Ray Powder Diffraction (XRPD) results for analysed arsenopyrite samples; α, γ = 90°. Location names are bold italic, and sample names in regular text. The at.% As was calculated from XRPD data according to [14]. Impurities were determined as an average of 15 SEM-EDS analyses.

Location/ Sample	a [Å]	b [Å]	c [Å]	β [°]	V [Å^3]	d_{131}	at.% As (XRPD)	Impurities [at.%] (SEM-EDS)
Rudnik								
Rud05/1	5.748(2)	5.680(2)	5.778(2)	112.09(1)	174.8(1)	1.63207(6)	33.346(1)	/
39	5.750(2)	5.685(2)	5.7744(16)	112.30(1)	174.95(9)	1.63248(5)	33.701(1)	/
Rujak								
GKC2017/03	5.750(7)	5.676(7)	5.768(7)	111.84(6)	174.7(4)	1.6330(1)	34.143(2)	0.7 Ni
GKC2017/04	5.751(3)	5.676(2)	5.769(2)	111.84(2)	174.8(1)	1.63138(6)	32.748(1)	0.3 Co, 1.5 Ni, 0.2 Sb
Drenjak								
T1-1	5.749(3)	5.684(3)	5.781(3)	112.13(2)	175.0(1)	1.63209(6)	33.363(1)	0.3 Co
T1-2	5.741(5)	5.679(5)	5.768(4)	112.25(1)	174.2(2)	1.6315(2)	32.861(3)	/
T1-6	5.743(2)	5.670(2)	5.772(2)	111.82(2)	174.5(1)	1.63071(3)	32.1674(6)	/
T1-22	5.745(2)	5.680(2)	5.774(2)	112.02(1)	174.6(1)	1.63172(6)	33.043(1)	/
Sastavci								
SST2017/04	5.747(2)	5.680(2)	5.777(2)	112.06(2)	174.8(1)	1.6322(1)	33.433(2)	/
SST2017/05	5.741(3)	5.685(4)	5.778(3)	112.04(3)	174.8(2)	1.63247(4)	33.6928(8)	0.3 Sb
SST2017/08	5.759(7)	5.685(7)	5.781(8)	112.22(6)	175.2(4)	1.6321(1)	33.346(2)	0.5 Sb, 0.4 Cu
Trepča								
Trepča 2	5.748(1)	5.677(2)	5.780(1)	112.07(1)	174.82(8)	1.63083(7)	32.271(1)	0.2 Sb
Golijskareka								
G.R. 7.1	5.749(2)	5.686(2)	5.775(2)	112.06(1)	174.97(8)	1.63318(4)	34.3086(8)	1.1 Co
Jurija								
CV-J2	5.748(2)	5.684(2)	5.776(2)	112.06(2)	174.9(1)	1.63304(5)	34.187(1)	4.3 Co

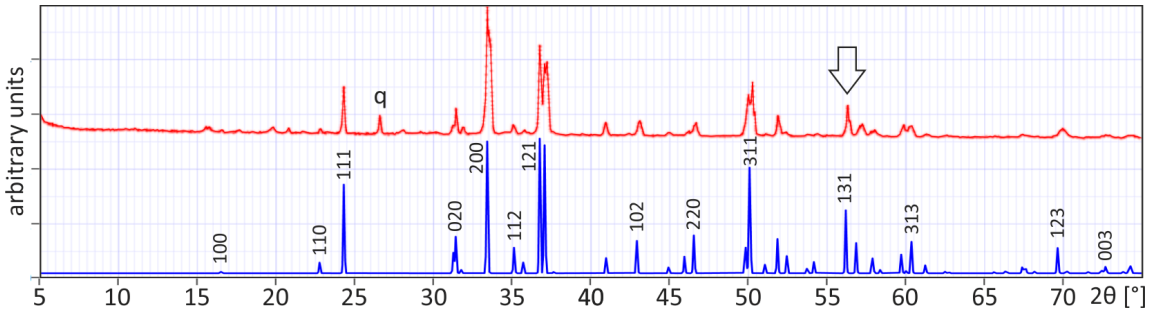

Figure 2. Experimental XRPD pattern of characteristic arsenopyrite sample from Drenjak (sample T1–22), compared with simulated XRPD pattern from [9]. The d_{131} peak, used for calculating at.% As in Table 1, is marked with an arrow. The additional diffraction peak at about $2\theta \approx 27^\circ$ belongs to quartz (q).

2.3. Transmission Electron Microscopy (TEM)

The FeAsS samples from the Drenjak deposit were cut, formatted, and mounted in epoxy resin. The surface was ground with emery papers according to the standard petrographical procedure [17] and pre-analysed with a polarising reflected-light microscope and SEM to identify the micro-location for TEM analysis. In the suitable grains, ⌀2.3 mm cores were extracted by the ultrasonic drill (Ultrasonic Cutter 380, Sonicut GmbH, Malsch, Germany), mounted by epoxy resin (G2, Gatan Inc., Pleasanton, CA, USA) in a ⌀3 mm brass tube, and sliced and polished into 100 µm disks. The disks were further thinned at the disk centre down to 10 µm (Dimple Grinder Mod. 656, Gatan Inc., Pleasanton, CA, USA) and Ar^+ ion-etched until perforation by a precision ion polishing system (PIPS Mod. 691, Gatan Inc., Pleasanton, CA, USA) at 4.5 keV and an incident angle of 8°. We chose the conventional Ar-ion etching for the TEM sample preparation over the site-specific focused ion beam (FIB) method to avoid possible Ga implantation during the sample preparation procedure.

The electron-transparent samples were mounted in a low-background dual tilt Be holder and analysed in the transmission electron microscope (TEM, JEM-2010F, JEOL Inc., Tokyo, Japan), operating at 200 kV and equipped with Energy-dispersive X-ray spectrometer (EDS, Link Pentafet mod. 6498, Oxford Instruments PLC, Abingdon, UK). Micrographs were recorded with a slow-scan CCD camera (Orius SC1000, Gatan Inc., Pleasanton, CA, USA) and processed and analysed by Digital Micrograph software (v3.1, Gatan Inc., Pleasanton, CA, USA).

3. Results and Discussion

3.1. X-ray Powder Diffraction (XRPD)

In total, 14 samples were analysed by X-Ray Powder Diffraction (XRPD), among them four specimens from the Drenjak locality (Figure 2). The cell parameters for investigated samples are summarised in Table 1, whereas the whole dataset is available in machine-reading format [18]. The average unit cell values calculated as a mean of 14 measurements are a = 5.748(06) Å, b = 5.680(85) Å, c = 5.775(42) Å, and β = 112.05(95)°. The calculated values for Drenjak locality, the mean of four measurements, are: a = 5.744(8) Å, b = 5.678(55) Å, c = 5.774(03) Å, and β = 112.05(65)°.

As reported in [19], the changes in the position of the (131) peak are a sensitive indicator of arsenopyrite composition. The (131) peak does not interfere with other reflections, has sufficient intensity, and can be precisely measured as it occurs at a relatively high 2θ. Based on 14 reliable XRPD measurements, the at.% As was calculated as at.% As = 866.67 d_{131}—1381.12 [14]. The XRPD study of arsenopyrite from four samples from Drenjak shows only slight variations in unit cell dimensions, d_{131}, and composition, i.e., As:S ratio. The calculated arsenic content is close to its theoretical value of 33.3 at.%; therefore, it can be said that the examined arsenopyrite from Drenjak shows almost ideal stoichiometry.

Otherwise, the As:S ratio in arsenopyrite can vary significantly, resulting in the As content ranging from less than 30 to 38.5 at.% [14]. Due to their homogeneity, absence of zoning, and stoichiometric composition, the samples from the Drenjak locality were selected for further TEM analyses (additional explanation and rationale regarding the selection of the samples can be found in Supplementary Information File S1).

Additionally, the samples from this locality are composed of crystals large enough for the conventional preparation of the oriented thin foils for TEM analyses.

3.2. Transmission Electron Microscopy (TEM)

The arsenopyrite samples are stable under an electron beam, allowing prolonged exposure without noticeable deterioration of the samples. The low-magnification overview micrographs revealed numerous planar defects parallel to the (010) plane, accompanied by a large surrounding strain (Figure 3a). Phase-contrast TEM micrographs (HR-TEM) reveal a coherent crystal structure with subtle moiré superlattice fringes in (211), manifested as an enhanced contrast ridges separated for ≈2 nm (Figure 3b). The chemical composition of the arsenopyrite crystal was analysed inside the TEM chamber by energy-dispersive X-ray spectroscopy (EDS). The quantification was assessed by the Cliff-Lorimer ratio thin section method (four iterations), with the Si-K line as the ratio standard element and line [20]. The calculated composition, mean of 16 spot analyses, was determined as (wt%): Fe 34, As 47, S 19 (sum 100); (at%): Fe 33.2, As 34.2, S 32.6; i.e., stoichiometric composition. The selected-area electron diffraction (SAED) pattern, recorded in the thin section of a large homogeneous grain, corresponded to single-crystal arsenopyrite and was indexed according to the structure data reported in [9] (Figure 3c).

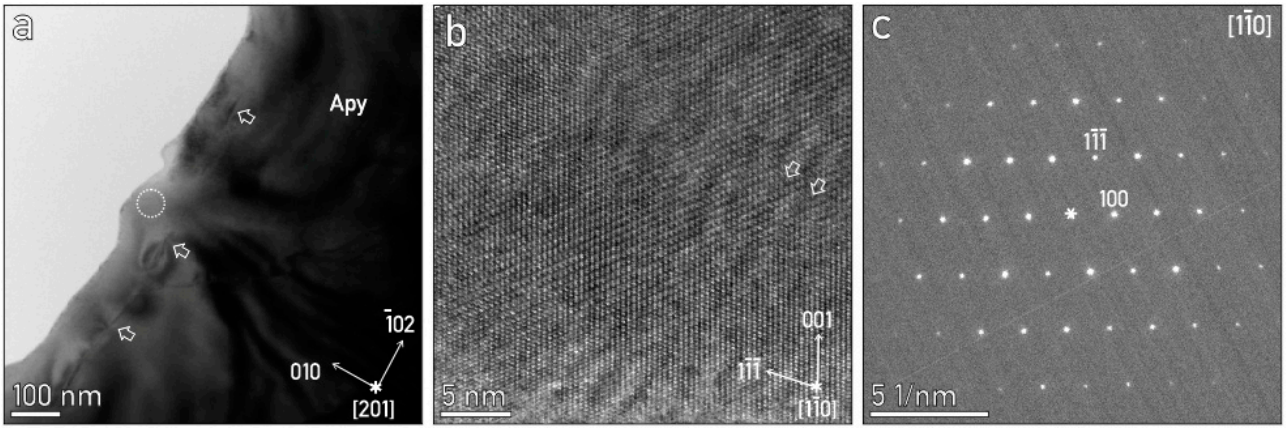

Figure 3. (**a**) Overview TEM micrograph of arsenopyrite (Apy) single crystal; arrows mark planar defects parallel to (010) plane; circle marks the SAED position. (**b**) HR-TEM of the bulk arsenopyrite sample viewed in [1–10], with marked main directions. White arrows mark a pair of moiré fringes. (**c**) SAED pattern recorded over (**b**) area, indexed for arsenopyrite structure from [9].

For investigated arsenopyrite, we calculated the unit cell parameters from SAED patterns, recorded in several different orientations (Table 2). Before analysis, the camera length (*L*) was calibrated by MAG*I*CAL traceable TEM calibration standard to enhance the method's precision. Quantitative analysis of electron diffraction was calculated according to Bragg's law $n\lambda = 2d \times \sin\theta$, using an approximation for small angles $2\theta = \sim\lambda/d = R/L$, with the final reduction $d = \lambda L/R$ [21]. Compared to the reported literature values, the calculated cell parameters for the investigated samples are summarised in Table 2. Using calibration standards, we significantly improved the precision of SAED, and we obtained a good match to the values reported in the literature. The values summarised in Table 2 are also in good agreement with the measured XRPD data summarised in Table 1.

Table 2. Reference values and experimentally measured unit cell parameters for arsenopyrite.

Ref.	a [Å]	b [Å]	c [Å]	β [°]	V [Å^3]	Symmetry	S.G.
[8]	9.51	5.65	6.42	90.0	344.956	monoclinic	$B2_1/d$
[19]	5.744	5.675	5.785	112.28	174.496	triclinic	P-1
[10]	5.741	5.649	5.756	110.588	174.750	monoclinic	$P\,2_1/c$
[9]	5.7612	5.6841	5.7674	111.721	175.456	monoclinic	$P\,2_1/c$
TEM study	5.75	5.68	5.76	111.5	175.03	monoclinic	$P\,2_1/c$

Further, the TEM methods allow for obtaining convergent beam electron diffraction (CBED) patterns for further insight into the crystal structure and direct microscopic observation of the structural features of the same region. The crystal structure of investigated arsenopyrite is closely related to the orthorhombic marcasite [10] and tetragonal rutile [9]. Our observations confirm a monoclinic crystal system, space group $P2_1/c$ [9]. As observed on the experimental Kikuchi lines image (Figure 4b,c), the whole pattern symmetry is *m* (Figure 4a,b), and the arsenopyrite crystal structure model derived from the TEM analysis closely resembles the marcasite prototype structure (Figure 4d). We interpret the occurrence of the forbidden *hk0* reflections (space-group absences) observed in the experimental SAED (Figure 4a) to occur due to twinning [10].

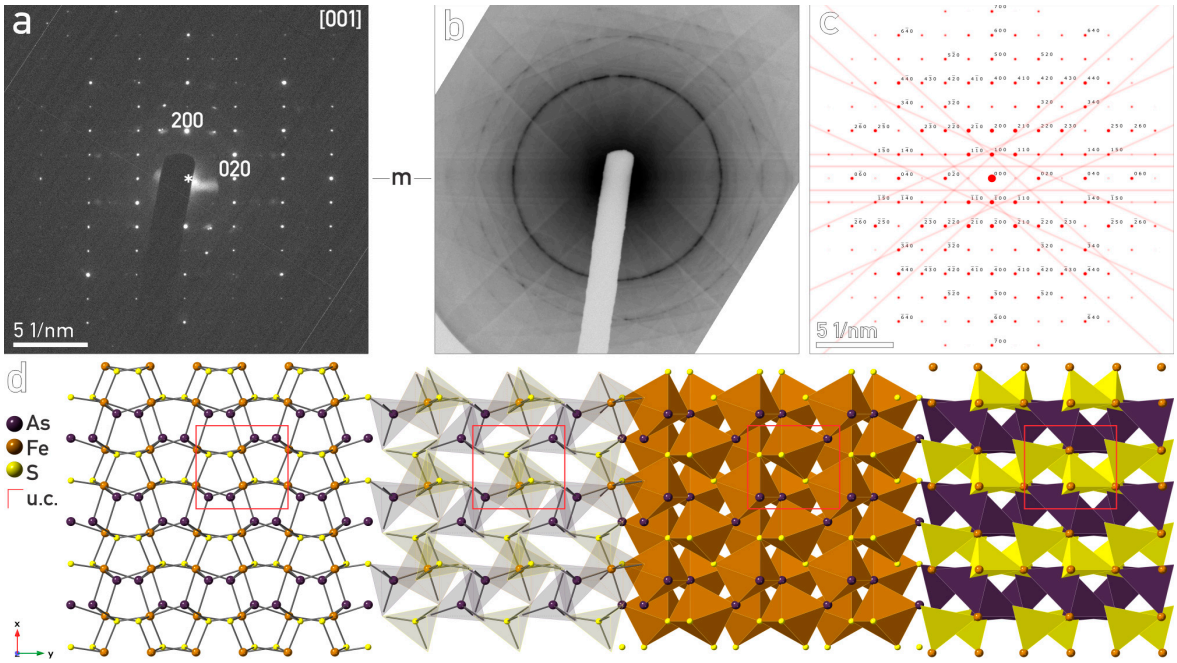

Figure 4. (**a**) SAED pattern indexed for arsenopyrite, with the corresponding (**b**) CBED pattern showing Kikuchi lines. (**c**) Simulated SAED and CBED (threshold 55%, intensity factor 1%, squares are space group absences). (**d**) Arsenopyrite crystal structure in the same orientation left to right: ball–stick model, coordination tetrahedra model, Fe-tetrahedra, and As- and S-tetrahedra models. The red square indicates the unit cell (u.c.).

For clarification, we analysed the regions of the arsenopyrite grains showing multiple planar structure defects resembling twin lamellae or periodic twin domains (Figure 5). According to the literature, the twinning in arsenopyrite is common in {100} and {001}, as contact or penetration twins in {101}, and in {012}, producing star-shaped trillings or cruciform twins [22]. Although arsenopyrite is monoclinic, such cyclic twinning can give it a pseudo-orthorhombic appearance [8]. In the investigated grains, we found 1-2 µm thick bands of successive parallel periodic polysynthetic {101} twinning, with individual lamellae on average 50 ± 15 nm thick, which are sharply terminated at the grain

boundaries (Figure 5a,b). The literature reports similar ≈ 100 nm thick lamellae, which were identified as localised Co exsolutions resulting in Co-poor arsenopyrite-type and Co-enriched cobaltite-type enrichment zones [10]. For verification, we investigated the local chemical composition by EDS analysis, which shows coherent, stoichiometric FeAsS chemical composition in both domain types without any deviation compared to the bulk grain. Additionally, the SAED patterns recorded over the multiple lamellae correspond to a single-phase arsenopyrite-type structure (Figure 5b′). Other planar defects following (22-1) planes (Figure 5c) can be interpreted as antiphase domains boundary (APB), with the displacement vector R 1/2 [100] and 1/2 [010] [10]; we observed such an example with a corresponding SAED pattern in the thin region of the larger twin-free grain (Figure 5d,d′).

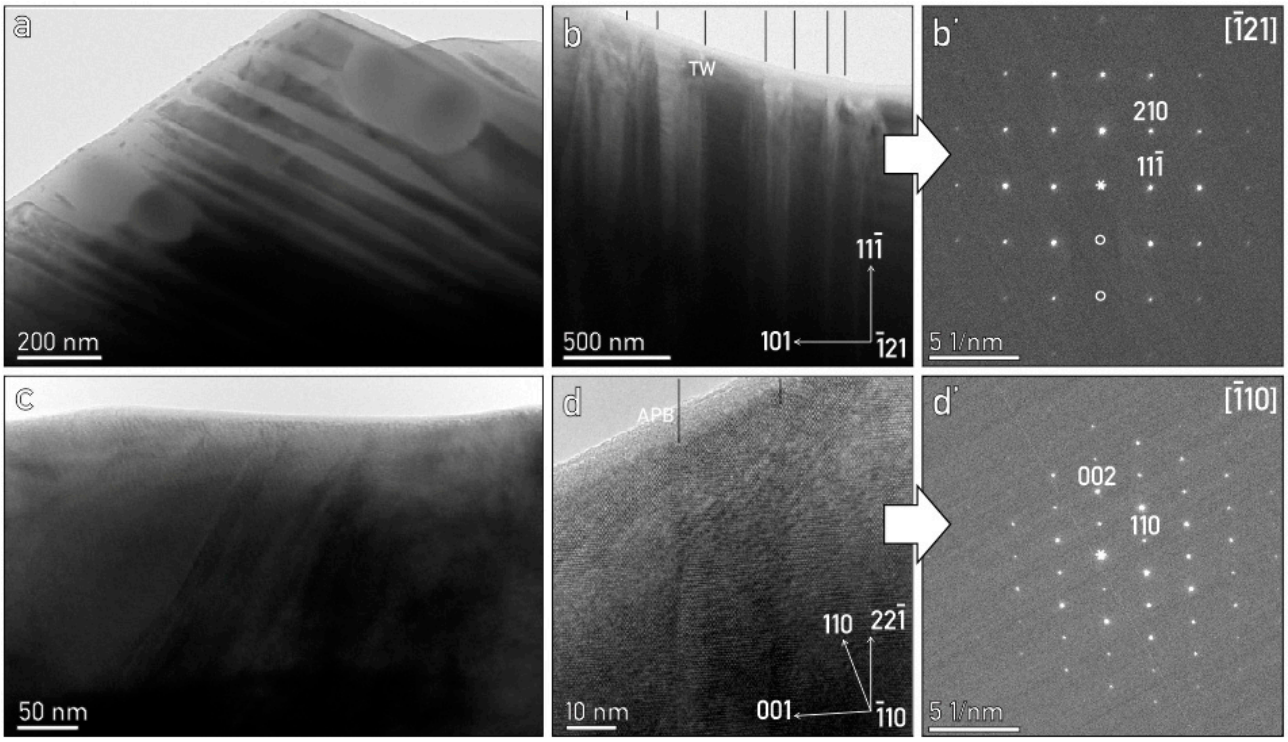

Figure 5. (**a**,**c**) Overview TEM micrograph of multiple parallel planar defects in single-crystal arsenopyrite. (**b**) Crystal viewed in [−121], showing {101} twin lamellae and corresponding (**b′**) SAED pattern; reflections masked by beam stopper are marked by white circles. (**d**) Arsenopyrite viewed in [−110] with antiphase domain boundary (APB) and corresponding (**d′**) SAED pattern.

On the thin edge of the arsenopyrite TEM samples that were exposed to air during sample manipulation, we observed a 6–7 nm thick crystalline epitaxial surface layer, topped by a ~1 nm amorphous layer (Figure 6a,b). The interface between pristine arsenopyrite and the surface layer is sharp, without any gradual transition that would suggest intermediate metastable phases. According to the EDS spot analysis, the crystalline layer is Fe- and As-rich oxide developed on the arsenopyrite surface upon air exposure during sample manipulation and transfer, ~30 min on air (additional experimental details are collected in the Supplementary Information File). The published results on the formation of surface oxides based on Auger depth profiling suggest, upon 30 min air exposure, the formation of a total 5 nm thick surface structure composed of three layers, starting with the top ~2 monolayers of FeOOH, followed by Fe_xAs_yO and $Fe_{1-x-z}As_{1-y}S$ [23], which does not coincide with our observations. A longer oxidation of 25 days resulted in the formation of a thicker layer, starting with 9 nm of oxygen and As-rich zone low in Fe and S, followed by 13 nm of an oxygen-deficient zone with a composition similar to bulk FeAsS [24]. Compared to our experimental observations, the crystalline epitaxial Fe-As-oxide layer with

the surface-most Fe-hydroxide amorphous layer is the most likely explanation. Inside the oxide layer, we did not observe any variation in the cell parameters, indicating a single-layer surface crystalline oxide structure with additional thin amorphous Fe-hydroxide on top. It is worth mentioning that such an oxidation structure was not observed on the samples directly transferred from the vacuum chamber to the TEM, with air exposure <5 min.

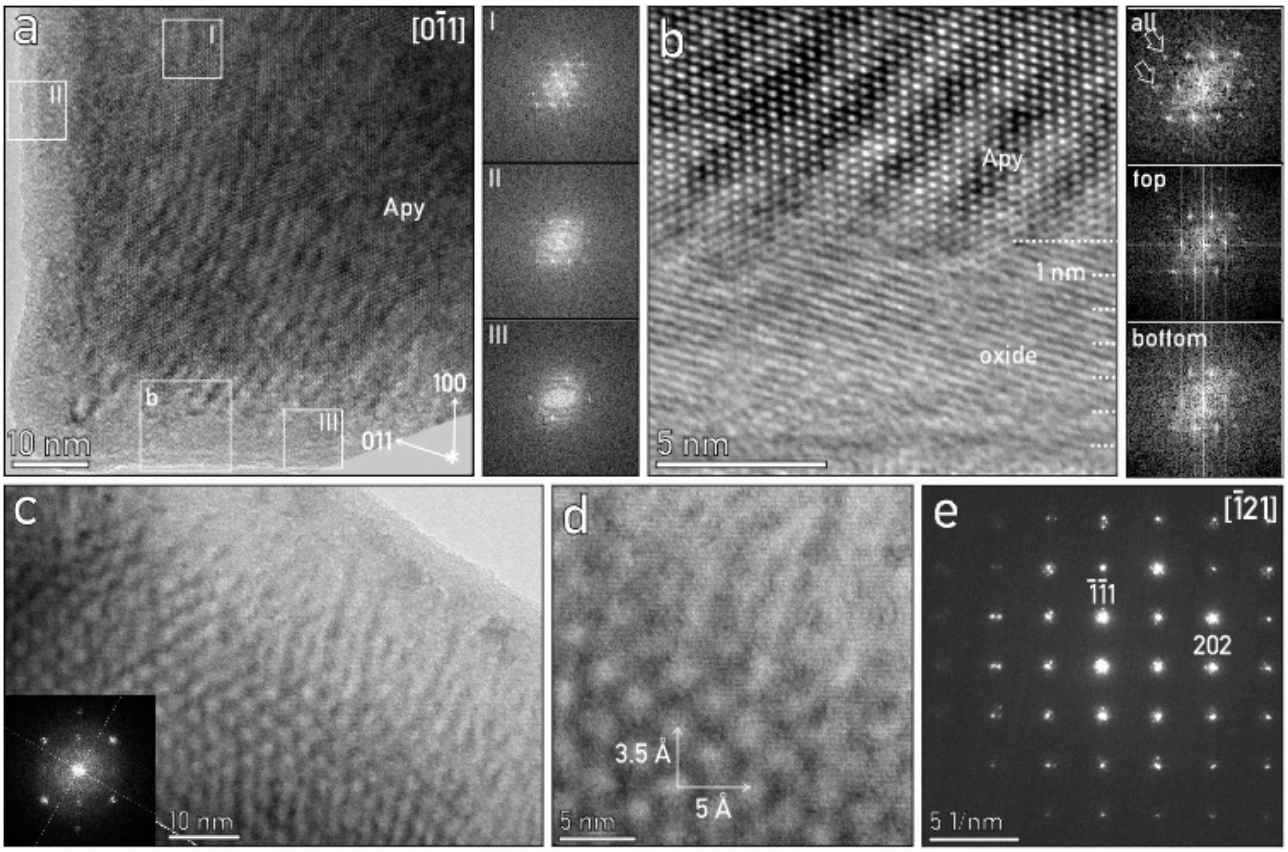

Figure 6. (**a**) Edge of arsenopyrite grain with marked regions for FFT patterns (I–III) and magnified (**b**) HR-TEM micrograph of the surface layer with corresponding FFT power spectra. (**c**) Overview TEM micrograph with corresponding FFT pattern, and (**d**) magnified detail with marked apparent 3.5 Å × 5 Å superlattice. (**e**) SAED pattern recorded over the same region, showing satellite reflections around each main diffraction peak. The main SAED pattern is indexed for arsenopyrite, and the additional oxide diffraction spots are slightly smaller due to the expanded unit cell parameters.

The crystalline surface layer manifests in complex moiré patterns with an apparent periodicity of 3.5 Å in {111} and 5 Å in {101} (Figure 6c,d). Similar superstructures were reported in several Cu-sulphides [25,26] and were interpreted as an ordered variation of the chemical composition, i.e., the periodic arrangement of impurities. This interpretation cannot be applied to our observations, as the chemical analysis by TEM-EDS shows no variation from the arsenopyrite stoichiometric composition besides elevated oxygen concentration (more details in Supplementary Information File S2). The possible explanation is that the moiré pattern results from an epitaxially aligned oxide layer developed on bulk arsenopyrite [27]. The SAED pattern recorded over both crystalline phases shows multiple satellite diffraction spots developed around the main diffraction peaks due to electron scattering on two aligned crystal structures with slightly different cell parameters (Figure 6e). The calculated values from the SAED pattern for the oxide layer show expansion in the interplanar distances of 3.5% in (100), 7.5% in (101), and 8.5% in (210) compared to the stoichiometric arsenopyrite structure.

The formation of an epitaxial oxide layer on the exposed arsenopyrite surface can present an obstacle for accurate electron and X-ray scattering diffraction measurements, especially for fine-powdered samples with a large surface-to-volume ratio [28]. Assuming the spherical shape of the particles and the observed speed of oxide formation, the detection limit of ~1% by volume criterion for a 5 nm thick surface oxide layer formed upon ~10 min air exposure is already achieved for 1.5 µm grains. As the standard XRPD sample is normally ground to a ~50 µm particle size, the 5 nm surface oxide presents 0.3 vol.%, while 30 nm thick oxide accounts for 1.8 vol.%, which is already enough to be detected by conventional XRPD. Therefore, the possible influence of the epitaxial superficial oxides affecting the accurate diffraction measurements has to be considered in the diffraction data interpretation.

4. Conclusions

We investigated the natural arsenopyrite crystals systematically sampled from the Šumadija-Kopaonik Pb-Zn/polymetallic ore district originating from different parageneses formed at higher to lower temperatures by XRPD and SEM methods. Samples from the Drenjak locality showed almost ideal stoichiometric composition and were further analysed by analytical TEM. The main conclusions, based on our experimental observations and interpretation, are:

- By studying arsenopyrite from different types of mineralisations in the Šumadija-Kopaonik ore area, no correlation was established regarding its composition and different deposition conditions, i.e., different mineral paragenesis.
- The average unit cell parameters measured by XRPD of near-stoichiometric arsenopyrite from the Drenjak locality, as a mean of four measurements, are a = 5.744(8) Å, b = 5.678(55) Å, c = 5.774(03) Å, $\alpha, \gamma = 90^{\circ}$, and ß = 112.05(65) °.
- The unit cell values calculated from the thin TEM sample using selected area electron diffraction (SAED) of the pristine, homogenous region of arsenopyrite crystal are a = 5.75 Å, b = 5.68 Å, c = 5.76 Å, $\alpha, \gamma = 90^{\circ}$, and ß = 111.5 °.
- TEM analysis of analysed arsenopyrite confirms a monoclinic crystal system, space group $P2_{1/c}$. We identified numerous polysynthetic {101} twinning with 50 ± 15 nm thick lamellae. The observed antiphase domain boundaries follow (22-1) planes.
- Upon exposure to air for t > 10 min, a surface crystalline oxide layer is formed. The surface oxide layer is epitaxial, with interplanar distances enlarged by 3.5%in (100) compared to the bulk arsenopyrite structure. The formation of oxides can be avoided by very short sample handling time on air (<5 min).

Supplementary Materials: The following supporting information can be downloaded at: https://www.mdpi.com/article/10.3390/cryst13020278/s1. The Supplementary Information File contains: Supplementary Information File S1: the rationale for selecting samples from the Drenjak locality for TEM analyses, and Supplementary Information File S2: TEM-EDS analysis of the oxidised and reference arsenopyrite sample (Figure S1).

Author Contributions: Conceptualisation, I.J., A.P. and J.Z.; methodology, J.Z. and A.Š. (Andreja Šestan); software, A.Š. (Aleš Šoster); validation, I.J., A.P., A.K. and J.Z.; formal analysis, I.J., A.K., A.Š. (Andreja Šestan) and J.Z.; investigation, I.J.; resources, A.P.; data curation, I.J. and J.Z.; writing—original draft preparation, I.J., A.P., A.K., A.Š. (Andreja Šestan), and A.Š. (Aleš Šoster); writing—review and editing, I.J., A.P., A.Š. (Aleš Šoster) and J.Z.; visualisation, J.Z.; supervision, A.P.; project administration, A.P.; funding acquisition, A.P. and J.Z. All authors have read and agreed to the published version of the manuscript.

Funding: This research was funded by the Slovenian Research Agency ARRS via the bilateral project Micro- to nano-scale textures of ore minerals: methods of study and significance, grant number BI-RS/18-19-035, project J2-4440 and program P1-0417.

Data Availability Statement: The data presented in this study are available on request from the corresponding authors. The results of XRPD analysis in machine-reading format are available from Mendeley Data, https://doi.org/10.17632/52v3sh67b5.1.

Acknowledgments: The authors acknowledge the problem identification and preliminary work of the late Predrag Vulić, from the University of Belgrade, Faculty of Mining and Geology, who started working on the issue of arsenopyrite crystal structure.

Conflicts of Interest: The authors declare no conflict of interest.

References

1. Vaughan, D.J.; Craig, J. *Mineral Chemistry of Metal Sulfides*; Cambridge University Press: Cambridge, UK, 1978.
2. Merkulova, M.; Mathon, O.; Glatzel, P.; Rovezzi, M.; Batanova, V.; Marion, P.; Boiron, M.C.; Manceau, A. Revealing the Chemical Form of "Invisible" Gold in Natural Arsenian Pyrite and Arsenopyrite with High Energy-Resolution X-ray Absorption Spectroscopy. *ACS Earth Space Chem.* **2019**, *3*, 1905–1914. [CrossRef]
3. Wang, Z.; Wang, Y.; Peng, E.; Zou, S.; Deng, T.; Lai, F.; Ning, J.; Dong, G.; Xu, D. Micro-Textural and Chemical Fingerprints of Hydrothermal Cobalt Enrichment in the Jingchong Co-Cu Polymetallic Deposit, South China. *Ore Geol. Rev.* **2022**, *142*, 104721. [CrossRef]
4. Chen, J.; Chen, Y.; Wei, Z.; Liu, F. Bulk Flotation of Auriferous Pyrite and Arsenopyrite by Using Tertiary Dodecyl Mercaptan as Collector in Weak Alkaline Pulp. *Miner. Eng.* **2010**, *23*, 1070–1072. [CrossRef]
5. Sung, Y.H.; Brugger, J.; Ciobanu, C.L.; Pring, A.; Skinner, W.; Danyushevsky, L.V.; Nugus, M. Erratum: Invisible Gold in Arsenian Pyrite and Arsenopyrite from a Multistage Archaean Gold Deposit: Sunrise Dam, Eastern Goldfields Province, Western Australia (Mineralium Deposita 10.1007/S00126-009-0244-4). *Miner. Depos.* **2009**, *44*, 793. [CrossRef]
6. Sidorova, N.V.; Aristov, V.V.; Grigor'eva, A.V.; Sidorov, A.A. "Invisible" Gold in Pyrite and Arsenopyrite from The Pavlik Deposit (Northeastern Russia). *Dokl. Earth Sci.* **2020**, *495*, 821–826. [CrossRef]
7. Cabri, L.J.; Newville, M.; Gordon, R.A.; Crozier, E.D.; Sutton, S.R.; McMahon, G.; Jiang, D.T. Chemical Speciation of Gold in Arsenopyrite. *Can. Mineral.* **2000**, *38*, 1265–1281. [CrossRef]
8. Buerger, M.J. The Symmetry and Crystal Structure of the Minerals of the Arsenopyrite Group. *Z. Für Krist.-Cryst. Mater.* **1936**, *95*, 83–113. [CrossRef]
9. Bindi, L.; Moëlo, Y.; Léone, P.; Suchaud, M. Stoichiometric Arsenopyrite, FeAsS, from La Roche-Balue Quarry, Loire-Atlantique, France: Crystal Structure and Mössbauer Study. *Can. Mineral.* **2012**, *50*, 471–479. [CrossRef]
10. Fuess, H.; Kratz, T.; Töpel-Schadt, J.; Miehe, G. Crystal Structure Refinement and Electron Microscopy of Arsenopyrite. *Z. Für Krist.-Cryst. Mater.* **1987**, *179*, 335–346. [CrossRef]
11. González-Jiménez, J.M.; Yesares, L.; Piña, R.; Sáez, R.; de Almodóvar, G.R.; Nieto, F.; Tenorio, S. Polymetallic Nanoparticles in Pyrite from Massive and Stockwork Ores of VMS Deposits of the Iberian Pyrite Belt. *Ore Geol. Rev.* **2022**, *145*, 104875. [CrossRef]
12. Goldmann, S.; Junge, M.; Wirth, R.; Schreiber, A. Distribution of Trace Elements in Sphalerite and Arsenopyrite on the Nanometre-Scale—Discrete Phases versus Solid Solution. *Eur. J. Mineral.* **2019**, *31*, 325–333. [CrossRef]
13. Maksimović, Z.; Divljan, S. The Results of Geological-Petrographic Mapping and Observation of Ore Occurrences in the Areas of Plana and Gokčanica on the Western Slopes of Željin. In *Book of Abstracts S.A.N. XXXIII.*; Geological Institute S.A.N.: Belgrade, Serbia, 1953; Volume 5, pp. 223–253.
14. Kretschmar, U.; Scott, S.D. Phase Relations Involving Arsenopyrite in the System Fe-As-S and Their Application. *Can. Mineral.* **1976**, *14*, 364–386.
15. Schmid, S.M.; Bernoulli, D.; Fügenschuh, B.; Matenco, L.; Schefer, S.; Schuster, R.; Tischler, M.; Ustaszewski, K. The Alpine-Carpathian-Dinaridic Orogenic System: Correlation and Evolution of Tectonic Units. *Swiss J. Geosci.* **2008**, *101*, 139–183. [CrossRef]
16. Šoster, A.; Zavašnik, J.; O'Sullivan, P.; Herlec, U.; Potočnik Krajnc, B.; Palinkaš, L.; Zupančič, N.; Dolenec, M. Geochemistry of Bashibos-Bajrambos Metasedimentary Unit, Serbo-Macedonian Massif, North Macedonia: Implications for Age, Provenance and Tectonic Setting. *Geochemistry* **2020**, *80*, 125664. [CrossRef]
17. Craig, J.R.; Vaughan, D.J. *Ore Microscopy and Ore Petrography*; Wiley-Interscience, Chichester and New York; John Wiley and Sons Ltd.: Hoboken, NJ, USA, 1981; ISBN 0471551759.
18. Jelić, I.; Pačevski, A.; Kremenović, A.; Šoster, A.; Šestan, A.; Zavašnik, J. XRPD Dataset of Arsenopyrite from Šumadija-Kopaonik Ore District. Mendeley online data repository. *Mendeley Data* **2023**. [CrossRef]
19. Morimoto, N.; Clark, L.A. Arsenopyrite Crystal-Chemical Relations. *Am. Mineral.* **1961**, *46*, 1448–1469.
20. Watanabe, M.; Williams, D.B. The Quantitative Analysis of Thin Specimens: A Review of Progress from the Cliff-Lorimer to the New ζ-Factor Methods. *J. Microsc.* **2006**, *221*, 89–109. [CrossRef] [PubMed]
21. Williams, D.B.; Carter, C.B. *Transmission Electron Microscopy: A Textbook for Materials Science*; Winter: New York, NY, USA, 2009; ISBN 9780387765006.
22. Goldschmidt, V.M. *Atlas Der Krystallformen: Plates and Text*; Winter: Heidelberg, Germany, 1913; ISBN 9788578110796.
23. Nesbitt, H.W. Oxidation States and Speciation of Secondary Products on Pyrite and Arsenopyrite Reacted with Mine Waste Waters and Air. *Mineral. Petrol.* **1998**, *62*, 123–144. [CrossRef]

24. Schaufuss, A.G.; Nesbitt, H.W.; Scaini, M.J.; Hoechst, H.; Bancroft, M.G.; Szargan, R. Reactivity of Surface Sites on Fractured Arsenopyrite (FeAsS) toward Oxygen. *Am. Mineral.* **2000**, *85*, 1754–1766. [CrossRef]
25. Owen, N.D.; Ciobanu, C.L.; Cook, N.J.; Slattery, A.; Basak, A. Nanoscale Study of Clausthalite-Bearing Symplectites in Cu-Au-(U) Ores: Implications for Ore Genesis. *Minerals* **2018**, *8*, 67. [CrossRef]
26. Ding, Y.; Veblen, D.R.; Prewitt, C.T. High-Resolution Transmission Electron Microscopy (HRTEM) Study of the 4a and 6a Superstructure of Bornite Cu_5FeS_4. *Am. Mineral.* **2005**, *90*, 1256–1264. [CrossRef]
27. Reidy, K.; Varnavides, G.; Thomsen, J.D.; Kumar, A.; Pham, T.; Blackburn, A.M.; Anikeeva, P.; Narang, P.; LeBeau, J.M.; Ross, F.M. Direct Imaging and Electronic Structure Modulation of Moiré Superlattices at the 2D/3D Interface. *Nat. Commun.* **2021**, *12*, 1290. [CrossRef] [PubMed]
28. Zavašnik, J.; Šestan, A.; Shvalya, V. Microscopic Techniques for the Characterisation of Metal-Based Nanoparticles. *Compr. Anal. Chem.* **2021**, *93*, 241–284. [CrossRef]